# Novel preparation strategy of graphdiyne ($C_nH_{2n-2}$): One-pot conjugation and S-Scheme heterojunctions formed with MoP characterized with in situ XPS for efficiently photocatalytic hydrogen evolution

Zhiliang Jin [*],[1], Youlin Wu [1]

*School of Chemistry and Chemical Engineering, Ningxia Key Laboratory of Solar Chemical Conversion Technology, Key Laboratory for Chemical Engineering and Technology, State Ethnic Affairs Commission, North Minzu University, Yinchuan 750021, PR China*

A B S T R A C T

As a new two-dimensional (2D) carbon hybrid material, graphdiyne has attracted much attention for its good electrical conductivity, tunable electronic structure and special electron transfer enhancement properties. With its unique atomic arrangement and 2D network of sp and $sp^2$ conjugated hybridization, graphdiyne has a natural advantage in building active catalytic sites. Meanwhile, its special charge distribution gives graphdiyne the ability to be an electron acceptor or donor. Due to its special properties, it has great potential in the field of hydrogen evolution for photocatalytic water decomposition. In this work, a novel strategy for the simple synthesis of graphdiyne ($C_nH_{2n-2}$) by $CaC_2$, hexabromobenzene and mixed organic solvents was firstly prepared and effectively enhanced the photocatalytic hydrogen evolution by topological semimetals (MoP). Combined with experimental tools such as in situ XPS, EPR and DFT calculations, the possible formation of S-Scheme heterojunctions between graphdiyne and MoP is proposed as an important strategy for the application of graphdiyne in the field of photocatalytic hydrogen evolution.

## 1. Introduction

To solve environmental problems and energy crises, photocatalytic $H_2$ evolution is one of the most promising responses [1–4]. Photocatalytic hydrogen evolution converts solar energy into a green, sustainable energy source (hydrogen) [5–7]. Semiconductor photocatalysts generate photogenerated electrons and holes under the excitation of sunlight, and some of the photogenerated electrons-hole migrate to the catalyst surface to participate in the redox reaction [8–10]. Although the sacrificial reagents can effectively consume electrons or holes in the half-reaction, the quick photogenerated electrons-hole makes the activity low [11–14]. The photocatalytic ability of catalysts can be effectively improved through the metal ion doping, metal deposition, supported group catalysts, controlled morphology, and construction of heterojunctions [15,16]. Among them, the supported co-catalysts can effectively reduce the accumulation of nano semiconductor materials and improve the exposure of active sites for the surface reaction [17–20]. The construction of heterojunctions can reduce the rate of photogenerated electrons-holes complexation and improve

photocatalytic activity [21–27]. Therefore, finding suitable materials with large specific surfaces is essential to enhance nanosemiconductor materials.

There are four types of photocatalysys frequently used in the field of photocatalysis: transition metal oxides, transition metal phosphides, metal sulfides, and metal-organic backbone materials (MOFs) [28–32]. Among them, transition metal phosphides have received wide attention because of their low cost and excellent catalytic performance in a hydrogen evolution reaction. In the preparrtion of transition metal phosphides, organic liquid phase, phosphorus source, and hydrothermal method are generally applied [33]. Among these transition metal phosphides, MoP and Pt have similar electronic structures, almost zero binding of H atoms, and a metal-like semiconductor. In the study of many researchers, MoP was obtained by mixing and grinding $MoO_3$ as precursor with $NaH_2PO_2 \cdot H_2O$ and calcining it under an $N_2$ atmosphere [34–36]. MoP does not perform as expected in photocatalytic hydrogen precipitation reactions because agglomeration and sintering occur during high-temperature phosphorylation and the exposed active sites are limited.
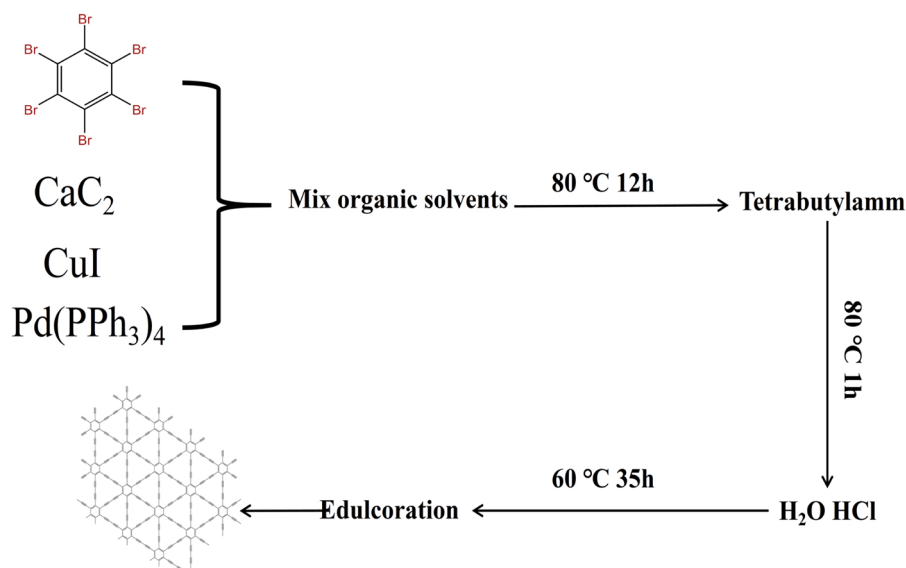
---

**Fig. 1.** Graphite acetylene (GDY) preparation diagram.

Graphdiyne (GDY) carbon material is an intrinsic semiconductor with a narrow band gap, which has great promise in photocatalysis. GDY is a novel of two-dimensional planar structure material after graphene ($sp^2$), carbon nanotube ($sp^2$), and fullerene ($sp^2$) [37–39]. GDY has a unique atomic arrangement and a two-dimensional network of conjugated hybridization of sp and $sp^2$ compared to conventional materials [40,41]. GDY has a natural advantage in constructing active catalytic sites. The particular charge distribution allows GDY to be an electron acceptor or donor, resulting in a catalyst with high catalytic activity and stability. Li et al. first grew GDY in situ on copper foil in 2010, which attracted many researchers to investigate the synthesis of GDY [42]. In 2018, Cui et al. used calcium carbide with hexabromobenzene for ball milling to prepare γ-graphyne [43].

In the present work, we prepared graphdiyne ($C_nH_{2n-2}$) by One-pot conjugation and S-Scheme heterojunctions formed with MoP as a new strategy for efficient photocatalytic hydrogen evolution. In the dye sensitized system (pH=10; 15 vol% triethanolamine; 10 mg eosin Y) 443.82 μmol (8876.4 $μmol·g^{-1}·h^{-1}$) hydrogen can be achieved in 5 h, which is 11.82 and 1.99 times higher than that of GDY and MoP, respectively. The composite catalyst has a more excellent hydrogen evolution than the single, It is shown that GDY can effectively inhibit the photogenerated electrons-holes complexation of MoP. The manuscript also reports a detailed description of the morphological structure, photoelectrochemical properties, and possible photocatalytic mechanism of the catalysts.

## 2. Experimental section

### 2.1. Preparation of MoP

Place 3.00 g $H_{24}Mo_7N_6O_{24}·4 H_2O$ in a clean crucible and react in a muffle furnace at a heating rate of 5 ℃/min for 4 h at 500 ℃ to obtain $MoO_3$. Grind 1 g $MoO_3$ with 5.00 g $NaH_2PO_2·H_2O$, placed in a ceramic boat, and reacted at a 3 ℃/min heating rate for 2 h at 300 ℃. After the reaction, the solid was washed five times by centrifugation with deionized water and anhydrous ethanol, which was then dried at 80 ℃ for 10 h. The sample MoP was obtained after aging for 3 months.

### 2.2. Preparation of graphdiyne (GDY)

The Fig. 1 briefly illustrates the preparation process of GDY, and the detailed process is as follows: 1.00 g of hexabromobenzene, 1.20 g of calcium carbide, 0.03 g of palladium catalyst (tetrakis(triphenylphosphine)palladium), 0.50 g of copper catalyst (cuprous iodide) were mixed as raw material, and mixed organic solvent (pyridine: tetrahydrofuran: toluene: ethyl acetate = 40:40:50:40) was added; the raw material and solvent were placed in a single mouth flask and reacted at 80 ℃ for 12 h. After adding 10 mL of tetrabutylammonium fluoride solution for 1 h at 80 ℃, 20 mL of deionized water and 10 mL of concentrated hydrochloric acid were added in turn and reacted at 60 ℃ for 35 h to obtain graphite diyne slurry. The graphdiyne slurry was rotary evaporated at 85 ℃ to get the viscous object and dispersed in anhydrous ethanol, and centrifuged by removing the high boiling point organic matter and copper catalyst by repeatedly anhydrous ethanol and dilute ammonia into the sediment to hot concentrated hydrochloric acid for one hour, filtered and dried to get graphdiyne (GDY).

### 2.3. Preparation of MoP/GDY (MG)

The preparation method of MoP/GDY is a classical physical mixing method. The Fig. 2 briefly illustrates the preparation process of MG, and the detailed process is as follows: in MoP/GDYX (MGX), X denotes the mass percentage of GDY with MoP. For instance, for the preparation of MG20, MG20 was obtained by weighing 0.02 g GDY and 0.10 g MoP in 40 mL of anhydrous ethanol, ultrasonically dispersing for 10 min, and stirring for 8 h. The stirred mixture was dried in a 70 ℃ oven for 8 h to obtain MG20.

### 2.4. Characterization

X-ray diffractometer (XRD) Rigaku Rint-2000 X-ray diffractometer system was used to determine the crystallinity of catalyst samples using copper Kα radiation. The crystallinity of catalyst samples was studied using X-ray diffraction (Rigaku Rint-2000 X-ray diffractometer equipped with copper Kα radiation (λ = 1.5406 Å). The successful preparation of GDY was demonstrated using Raman spectroscopy and Fourier transform infrared spectroscopy. Scanning electron microscopy (SEM, JSM-6701 F JEOL) and transmission electron microscopy (TEM, JEM-2100) were used to understand the morphological characteristics of the samples further. X-ray photoelectron spectroscopy (XPS, ESCALAB 250Xi) and Shimadzu spectrophotometer (UV-2550, $BaSO_4$ as reference background) were used to determine the valence and UV-Vis diffuse reflectance measurements of surface elements. Photoluminescence (PL) and time-resolved photoluminescence (TRPL) experiments were performed
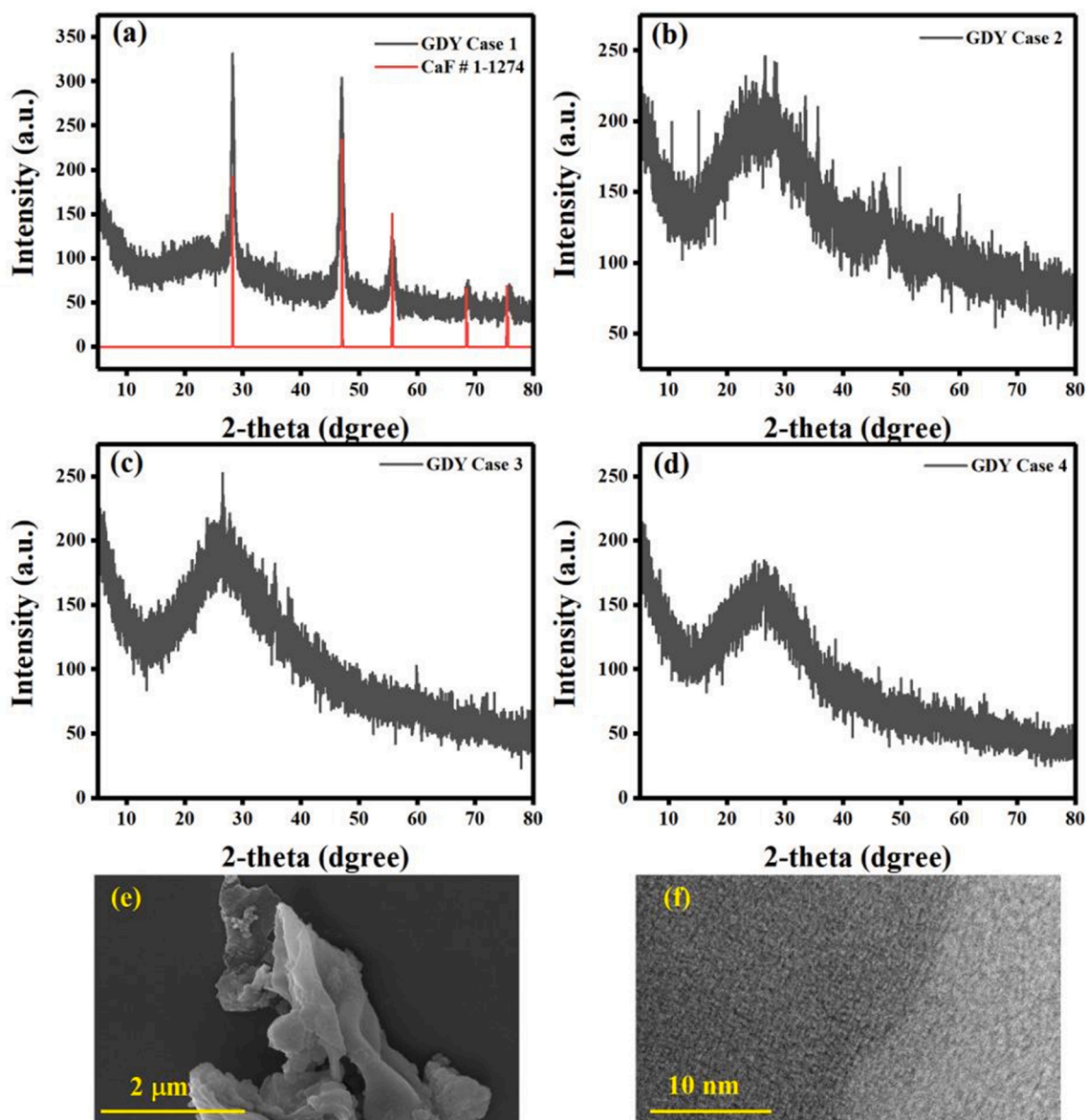
**Fig. 2.** XRD patterns of (a-d) GDY Case 1–4; (e) SEM images of GDY Case 4; (f) TEM image of GDY Case 4.

**Table 1**

Contrast with classical organic synthesis methods.

| Name | Chemical reagents | Preparation time | Re. |
|------|-------------------|------------------|-----|
| Organic Total Synthesis | $Br_6C_6$, $Pd(PPh_3)_4$, Trimethyl silyl acetylene, Ethyl acetate, Pyridine, Furan, Toluene,Tetrabutylammonium fluoride, n-butyllithium, anhydrous zinc chloride, etc. | 7 day | [42] |
| One Pot Method | $CaC_2$, $Br_6C_6$, CuI, $Pd(PPh_3)_4$, Ethyl acetate, Pyridine, Furan, Toluene, Tetrabutylammonium fluoride | 2 day | This work |

on the samples using a steady-state spectrometer (FluorOMax-4, HORIBA) and a single photon counting controller (Floor Hub, Floor Center). Electrochemical experiments were performed on an electrochemical workstation (VersaSTAT4–400, AMETEK). Electronparamagneticresonance (EPR) experiments were performed on an electron paramagnetic resonance spectrometer (Bruker A300). Kelvin Probe Force Microscope (KPFM) experiments were performed on

German Bruker Dimension Icon.

*2.5. Hydrogen production experiments*

The photocatalyst, dye sensitizer, and sacrificial reagent were packed into a 60 mL glass vial, and nine channels were used for the photocatalytic reaction (PCX50A Discovery System). The procedure is as follows. First, 10 mg of MG20 and 10 mg of the photosensitizer (EY) were uniformly dispersed in 30 mL of TEOA solution (15 vol%). Then, the solution was sonicated for 3 min to make it uniformly distributed, nitrogen was injected into the glass vial, and hydrogen production experiments were performed in 9 channels after air was expelled from the reaction vial. Finally, gas chromatography measured hydrogen production (TianmiGC00, TCD/13X column, $N_2$ as carrier gas), and 0.5 mL of gas was extracted from the glass vial per hour. The optimal hydrogen production environment for MG20 was determined by studying the hydrogen production of MG20 at different pH values for 5 h. Starting with the second cycle, each cycle was preceded by eliminating hydrogen from the previous process and supplemented with 5 mg EY.
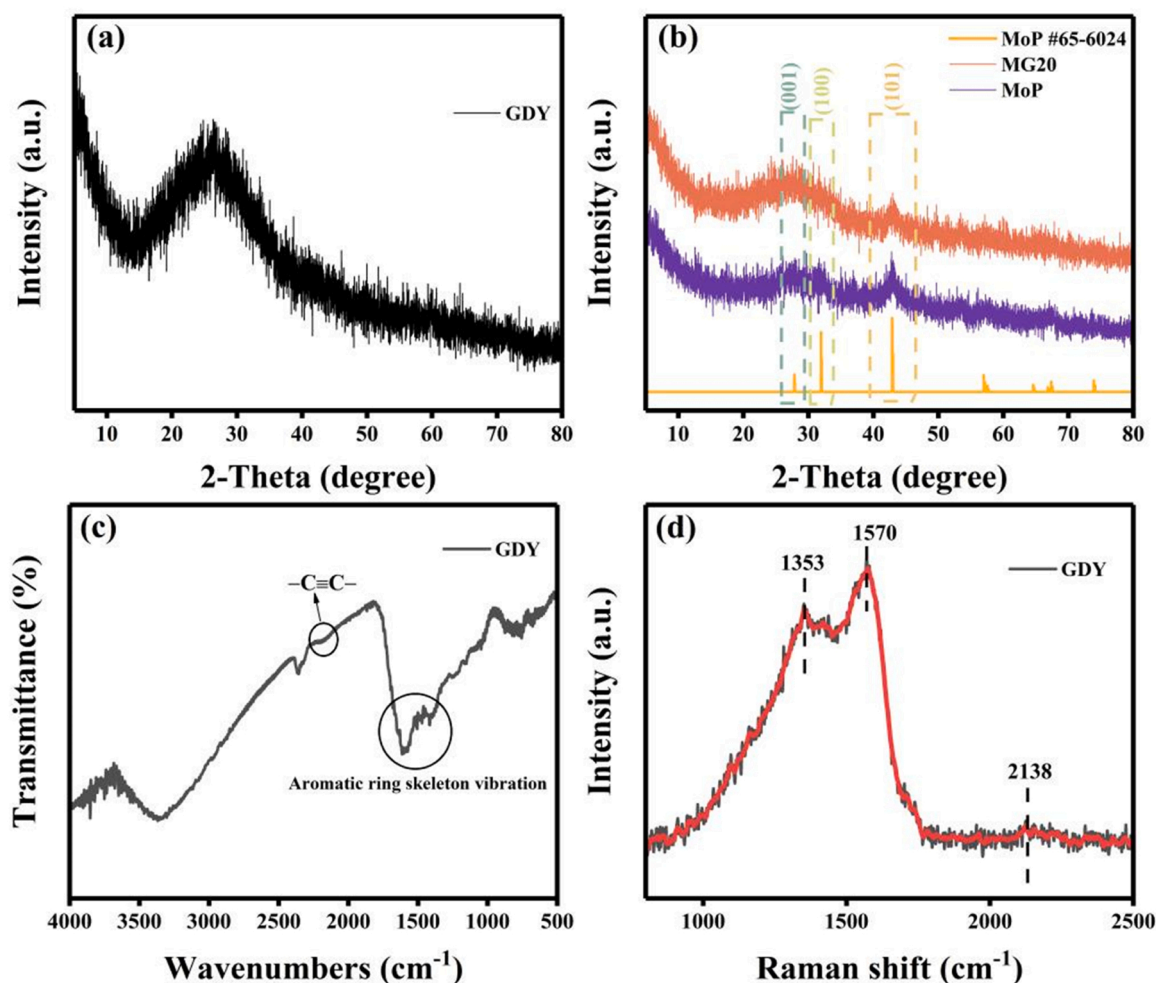
**Fig. 3.** XRD patterns of (a) GDY; (b) MoP, and MG20; (c) FT-IR spectra of GDY; (d) Raman spectrum of GDY.

## 2.6. Electrochemical experiments

A typical three-electrode system (saturated glycolic electrode, platinum electrode, and working electrode made of ITO conductive glass). The electrode sheet was created by dispersing 5 mg of catalyst in 0.5 mL of adhesive (Nafion: ethanol = 1: 9), ultrasonically dispersing it well, and drying it after uniformly coating it into a $1 \times 1$ area on $1 \times 2$ ITO indium tin oxide conductive glass. The electrolyte is a 0.2 mol/L $Na_2SO_4$ solution. The incident light source is a 300 W xenon lamp.

## 2.7. Electronparamagneticresonance (EPR (DMPO-O$_2^-$)) experiments

The test process is as follows: take 5 mg catalyst powder dispersed in 10 mL of methanol, after ultrasonic shaking for 5 min, take 200 microliters of mixed solution, add 200 microliters of 5,5-dimethyl-1-pyrroline N-oxide (DMPO) solution with a concentration of 100 mM, mix and shake well, put it into a capillary tube and then put it into a glass tube into the machine test, room temperature, divided into dark and light test. Generally, the default lighting is tested after 5 min

## 3. Results and discussion

### 3.1. Exploration of GDY preparation

It is important to achieve optimization of the experimental results by changing the experimental conditions. In this regard, the author lists

several experimental cases explored. Case 1 The drug dosage was unchanged and the reaction conditions were changed as follows: 5 h of reaction at 80 ℃ and 23 h of reaction at 60 ℃ without treatment with hot concentrated hydrochloric acid. Case 2 The amount of drugs remained unchanged and the reaction conditions were changed as follows: 5 h reaction at 80 ℃, 23 h reaction at 60 ℃, 0.5 h treatment with hot concentrated hydrochloric acid. Case 3: The dosage of drugs remained unchanged, and the reaction conditions were changed as follows: 12 h at 80 ℃, 23 h at 60 ℃, and 1 h with hot concentrated hydrochloric acid. Case 4, the dosage of drugs remained unchanged and the reaction conditions were changed as follows: 12 h at 80 ℃, 35 h at 60 ℃ and 1 h with hot concentrated hydrochloric acid. XRD patterns of GDY Case X (X = 1;2;3;4) were obtained (Fig. 2(a-d)). It can be clearly observed that with changing the reaction conditions, and post-treatment, the XRD patterns of the samples showed amorphous carbon peaks. Meanwhile, the SEM and TEM images of GDY Case 4 can reveal that GDY is an amorphous lamellar material (Fig. 2(e-f)). Table 1 shows the cost and time comparison between this method and classical organic synthesis.

### 3.2. Structural and morphological analysis

XRD analyzed the crystal structures of GDY, MoP, and MG20. In Fig. 3(a, b), pure GDY is an amorphous carbon material, and MoP has relatively prominent XRD diffraction peaks at $2\theta = 27.86°$, $31.97°$, and $42.90°$, which are caused by the (001), (100) and (101) crystallographic
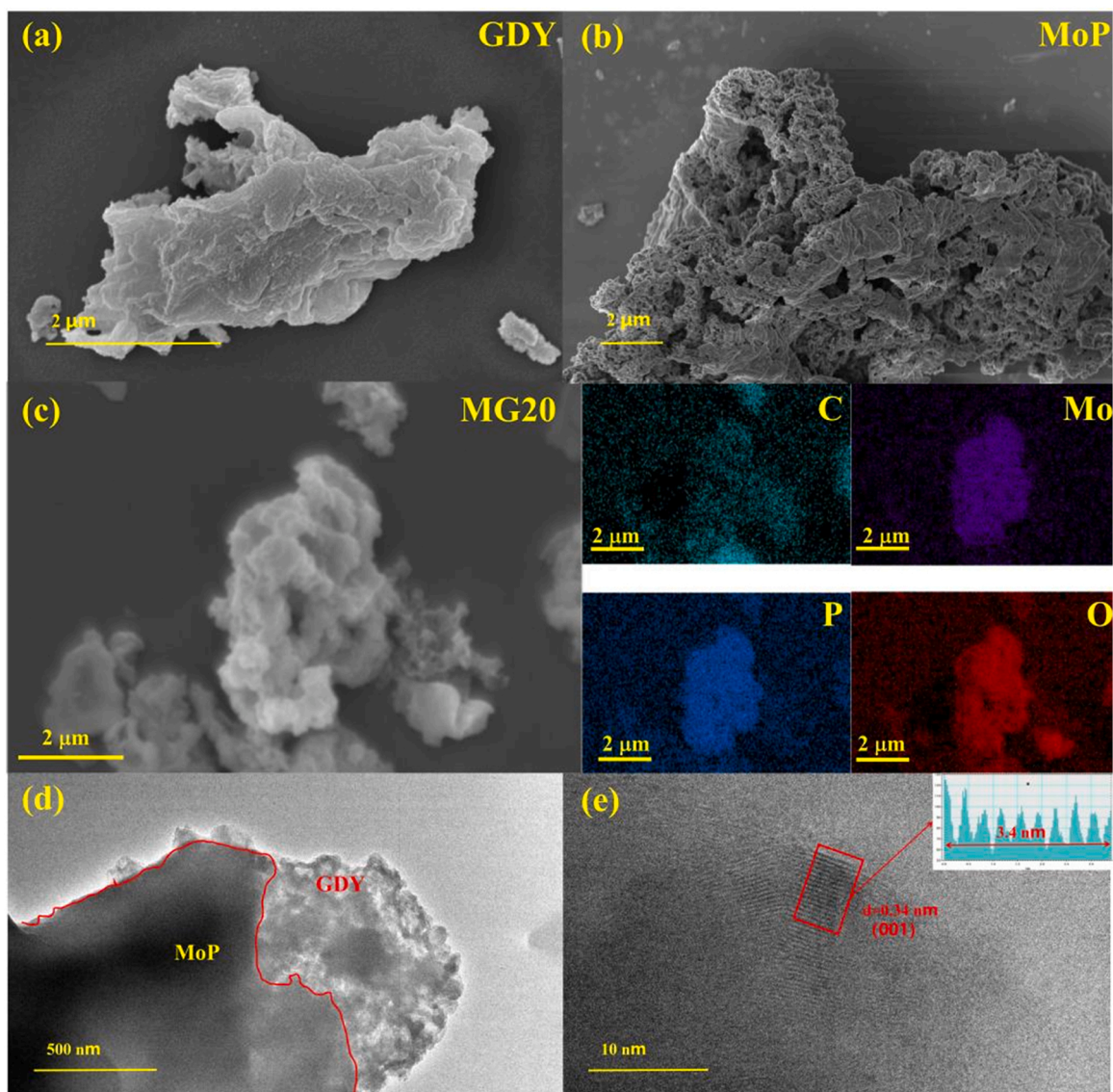
**Fig. 4.** SEM images. (a) GDY; (b) MoP; (c) SEM mapping smages of MG20; (d) TEM smages of MG20; (d) HRTEM smages of MG20.

surfaces of MoP. Since the GDY sheet covers the surface of MoP, the intensity of the XRD diffraction peaks of MoP is further reduced. In the FT-IR spectrum of GDY (Fig. 3(c)), the two absorption bands at 1413 and 1600 cm$^{-1}$ are due to the skeletal vibration of the aromatic ring [44], and the absorption band at 2187 cm$^{-1}$ is due to the stretching vibration of C≡C [45–47]. Raman spectra further demonstrate (Fig. 3(d)) that the characteristic peaks at 1353 and 1570 cm$^{-1}$ are from the G and D bands of sp$^2$ carbon. The unique distinct height at 2138 cm$^{-1}$ is due to the conjugated double acetylene linkage vibration (-C≡C-C≡C-). It is shown that GDY can be effectively prepared by using the one-pot conjugation method.

The morphological characteristics of GDY, MoP and MG20 were investigated by SEM. As shown in Fig. 4(a, b), GDY is a lamellar structure and MOP is a porous block sintered together. By scanning the surface elements of MG20 (Fig. 4 (c)), MoP and GDY are distinguished by the distribution of C, Mo and P elements. Also, GDY can be seen attached to the surface of MoP by the distribution of elements.The distinction between GDY and MoP components in MG is performed by TEM in Fig. 4 (d). A clear lattice stripe is observed in Fig. 4(e), which is found to be attributed to the (001) crystal plane of MoP by measurement (d = 0.34).

The XPS evaluated the surface elemental valence and chemical

composition of GDY, MoP, and MG20 photocatalysts. In Fig. 5(a), the C 1 s orbitals of pure GDY correspond to C-C(sp$^2$) and diacetylene bonds (285.0 eV) for C-C(sp), C-O (286.0 eV) and C=O (287.0 eV), respectively [48,49]. The same corresponding C-element effect is observed in MG20, and the composite sample is shifted in the direction of reduced binding energy for C-C(sp$^2$) and C-C(sp). The high-resolution spectrum of Mo 3d can be decomposed into four peaks (Fig. 5(b)). The peak at 228.1 eV is attributed to Mo$^{\delta+}$ of MoP ($0 < \delta < 4$), and the peaks at 223.1 eV and (233.0, 235.7 eV) are attributed to Mo$^{4+}$ and Mo$^{6+}$, respectively, which are typical of MoO$_2$ and MoO$_3$, respectively [50–53]. In the high-resolution spectrum of P 2p (Fig. 5(c)), two peaks located at 129.2 (2p$_{3/2}$) and 130.1 eV (2p$_{1/2}$) are attributed to MoP, respectively. in addition, there is an intense peak at 134.1 eV, which is a P-O species due to surface oxidation [54,55]. In the high-resolution spectrum of the composite catalyst, Mo 3d and P 2p are shifted in the direction of increasing binding energy, where the shift of the P-O species is almost zero. In the high-resolution spectrum of O 1 s (Fig. 5(d)), three peaks are present at 531.7, 533.2, and 535.8 eV, attributed to the lattice O of the sample, oxygen in oxygen vacancies,s, and the adsorbed water surface, respectively [56,57]. Because there is a certain interaction force between GDY and MoP at their contact surface, which results in a charge
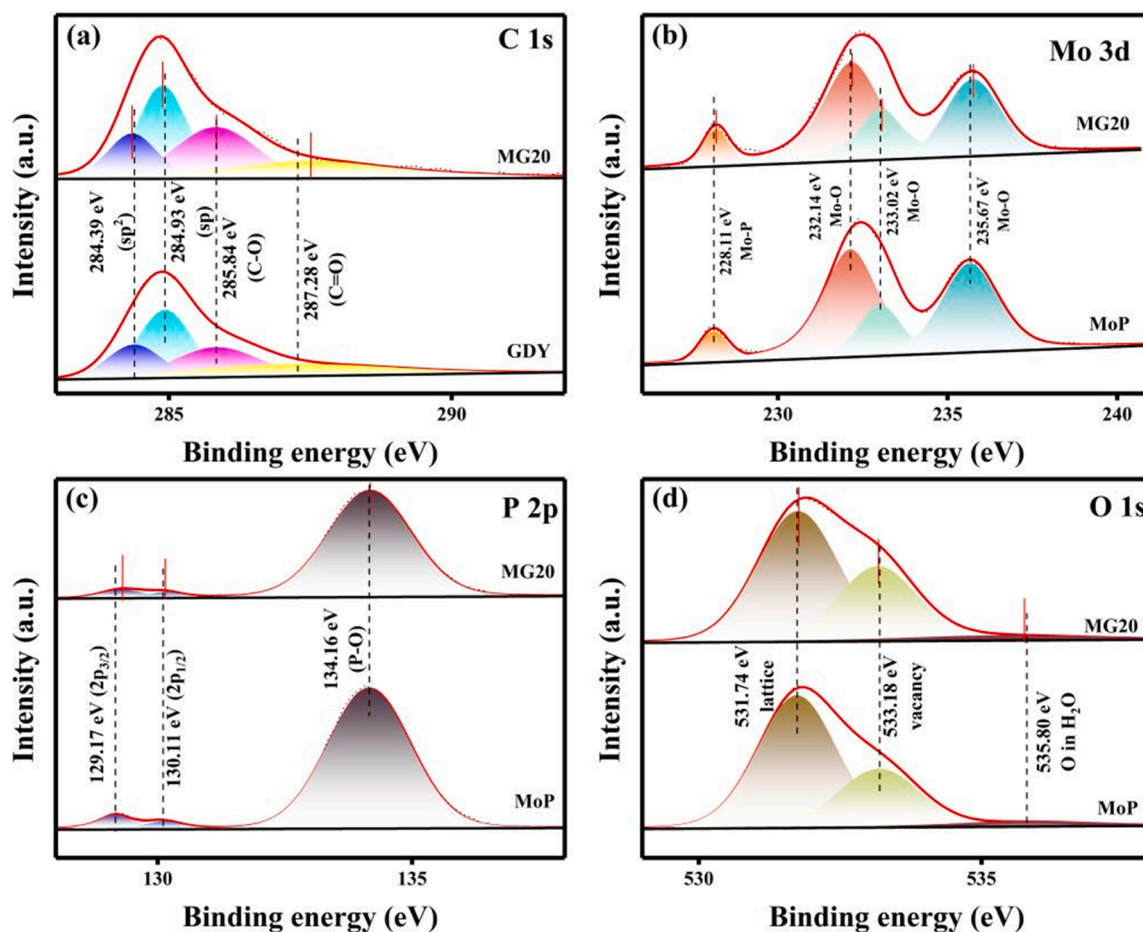
**Fig. 5.** XPS spectra of (a) C1s; (b) Mo 3d; (c) P 2p; (d) O 1 s.

balance between the contact surfaces, leading to a shift in binding energy between the composite catalyst and the single catalyst.

### 3.3. Photocatalytic performance analysis

The photocatalytic hydrogen precipitation experiments are the best evidence to evaluate the hydrogen evolution ability of the photocatalyst (TEOA (15%, pH=10) as sacrificial reagent and eosin Y (EY) as photosensitizer). In Fig. 6(a, b), the most strongest hydrogen evolution capacity can reach 443.82 μmol (8876.4 μmol·g$^{-1}$·h$^{-1}$) H$_2$ in 5 h when the mass of GDY is 20% of the group mass of the MoP, which is 1.99 and 11.82 times higher than that of MoP and GDY, respectively. The reason for this $1 + 1 > 2$ case is that MoP and GDY do not carry out photocatalytic hydrogen precipitation reaction independently of each other, but there is a mutually favorable positive interaction, which improves the hydrogen evolution ability of the catalyst. In the environment of sacrificial reagent through different pH values (Fig. 6(c)), there is a strong hydrogen evolution ability at pH= 9–10. The hydrogen evolution performance of MG20 at pH= 8 was only 81.1% of that under the optimal environment. The hydrogen precipitation ability of MG20 at pH= 11 decreases sharply, and the hydrogen evolution ability at pH= 12 is only 1.8% of pH= 10. This is due to the low content of free protons in the system at higher pH, which is not conducive to photocatalytic hydrogen production reaction [58,59]. In the same way, the protonation of TEOA at lower pH leads to the weakening of the electron donor capacity of TEOA [60,61]. In Fig. 6(d), the experiments on the cyclic hydrogen evolution capacity of MG20 were performed starting from the second experiment with 5 mg of EY supplementation each time

(half of the first cycle). It can be noticed that the 10th, 15th, and 20th hours are 78.1%, 68.1%, and 64.5% of the 5th hour. Previous studies on the effect of EY content on the catalyst's hydrogen evolution capacity [44–46], attributed this phenomenon to the depletion of EY and the shielding effect on light. Table 2 shows a simple comparison of the recently published graphdiyne-based composites with this work.

### 3.4. Optical and Electrochemical performance

The Fig. 7(a) depicts the test results of the UV-Vis diffuse reflectance spectra of GDY, MoP, and MG20. It can be seen from Fig. 7(a) that GDY, MoP, and MG20 all have strong light absorption ability. The band gap of GDY and MoP can also be obtained by the Kubelka-Munk method (Fig. 7 (b)); the results showed that the band gap (E$_g$) of GDY and MoP is 1.56 and 1.64 eV. When light hits some atoms, the energy of the light causes some electrons around the nucleus to jump from their original orbitals to higher energy orbitals. From the ground state to the first excited single-line state or the second excited single-line state, etc. The first exciting single-line state or the second excited single-line state, etc. is unstable, so the ground state is restored. When the electrons are restored from the first excited single-line state to the ground state, the energy is released in the form of light, so fluorescence is produced. Therefore, the photogenerated electrons-holes complexation rate of photocatalysis can be determined by quantitative analysis through PL. Fig. 7(c) shows the PL of the photocatalyst with an emission wavelength of 480 nm and an excitation wavelength of 537 nm. The fluorescence intensity of pure GDY is the lowest, indicating that GDY's photogenerated electrons-holes complexation rate is low. As expected, the fluorescence intensity of
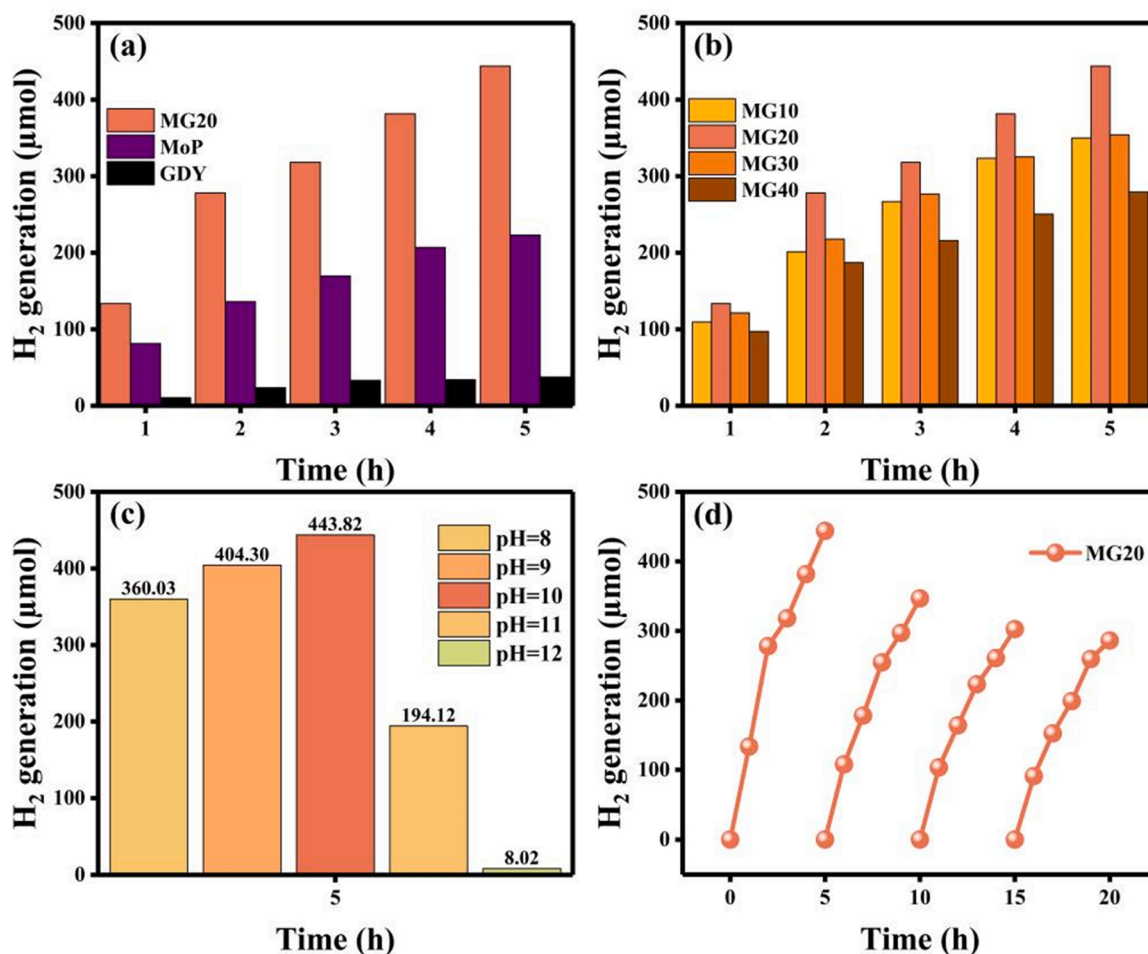
**Fig. 6.** (a) hydrogen evolution of GDY, MoP, and MG20 catalyst; (b) Hydrogen evolution of MGX; (c) Hydrogen evolution of MG20 at different pH values; (d) Hydrogen production cycle curves of MG20.

**Table 2**
Comparison of graphdiyne-based composites.

| Samples | Environmental system | Hydrogen evolutionary capability | Graphdiyne preparation method | Re. |
|---|---|---|---|---|
| $Mn_{0.2}Cd_{0.8}S$/graphdiyne/CuI | $Na_2S+Na_2SO_3$ | $10\ mmol \cdot g^{-1} \cdot h^{-1}$ | Organic total synthesis | [62] |
| graphdiyne/$Co_3O_4$ QDs | Photosensitization system (20 mg EY) | $1501\ \mu mol \cdot g^{-1} \cdot h^{-1}$ | Organic total synthesis | [63] |
| MG20 | Photosensitization system (10 mg EY) | $8876\ \mu mol \cdot g^{-1} \cdot h^{-1}$ | One-pot method | This work |
| $MoO_2$/graphdiyne/CuI | Photosensitization system (10 mg EY) | $820\ \mu mol \cdot g^{-1} \cdot h^{-1}$ | Organic total synthesis | [64] |
| MIL-53(Al)/graphdiyne/CuI | Photosensitization system (10 mg EY) | $243\ \mu mol \cdot g^{-1} \cdot h^{-1}$ | Organic total synthesis | [65] |

MG20 was lower than that of MoP, indicating that the mixture of MoP and GDY could effectively inhibit the photogenerated electrons-holes complexation of the MoP catalyst. The fitted data for EY, GDY, MoP, and MG20 are in Table 3 (Fig. 7(d)). The average lifetime of MG20 is 1.22 ns, which is significantly higher than that of EY (1.17 ns), GDY (1.16 ns), and MoP (1.15 ns). The combination of MoP and GDY can effectively prolong the catalyst photogenerated carrier lifetime, which can improve the efficiency of carrier migration to the catalyst surface.

To further understand the electron transfer performance of MG20, the variation in the electron transfer performance of MG20 is compared with MoP and GDY. We can see that MG20 has the highest photocurrent density compared to a single cayalyst (Fig. 8(a)). With increasing time, the photocurrent density of both MoP and MG20 decreases, which is due to the accumulation of photogenerated holes on the electrode surface, resulting in the absorption of photogenerated electrons by the catalyst. The smaller the arc radius of the Nyquist curve, the smaller the

impedance value. In Fig. 8(b), the arc radius of MG20 is smaller than that of MoP, which indicates that loading GDY on the surface of MoP can effectively reduce the charge transfer impedance, the charge transfer rate of MG20 is significantly higher than that of pure MoP. In the LSV curves of GDY, MG20, and MoP (Fig. 8(c)), the hydrogen precipitation overpotential of GDY, MG20, and MoP increases sequentially, resulting in MG20 being more prone to hydrogen precipitation reaction than MoP. From the cyclic voltammetric curves of GDY, MG20, and MoP (Fig. 8 (d)), it can be seen that MG20 has both properties of GDY and MoP. In addition, MG20 has a more pronounced redox peak and larger absolute area than MoP, which indicates that GDY can effectively reduce the electrons-holes recombination rate of MoP.

### 3.5. Energy band structure

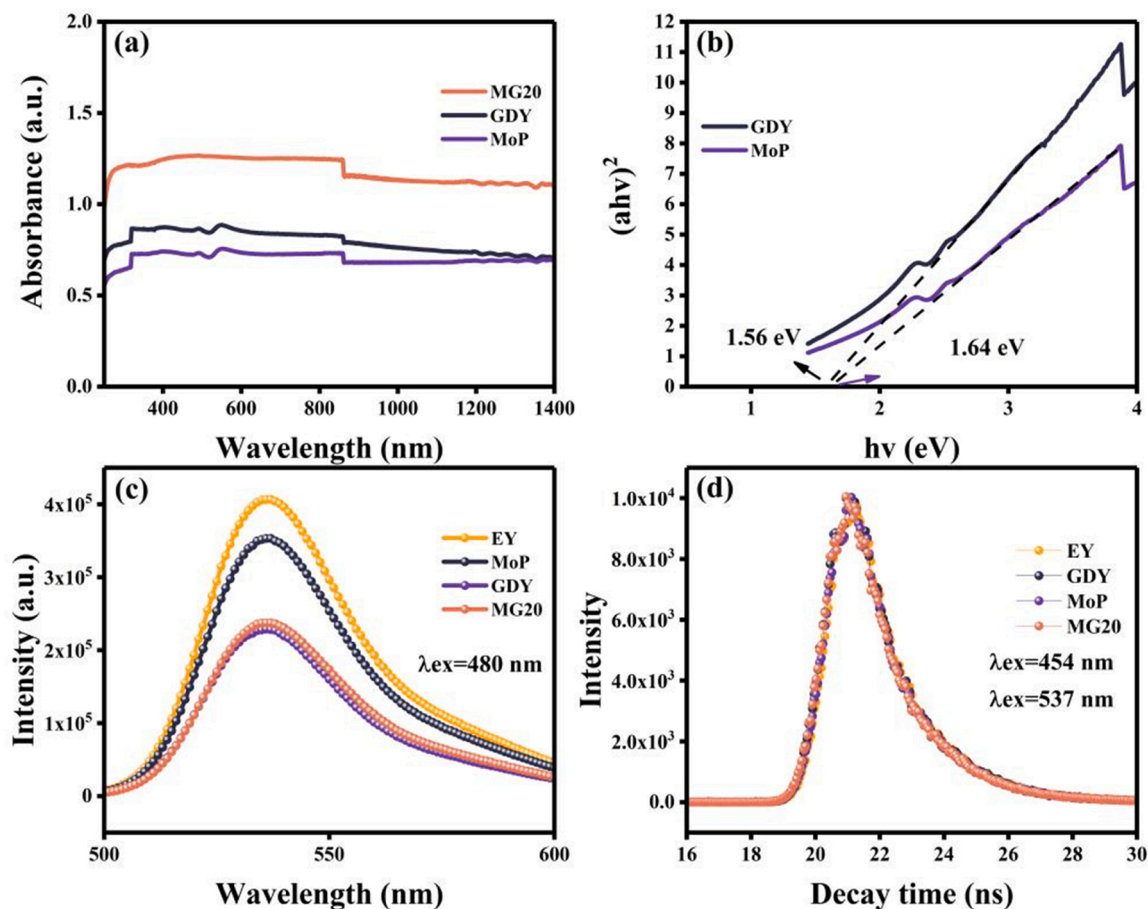To further understand the possible mechanism between MoP and

**Fig. 7.** (a) The UV–vis absorption spectra; (b) The forbidden bandwidth; (c) Photoluminescence spectra; (d) Time-resolved photoluminescence spectra.

**Table 3**
Time-resolved photoluminescence fitted data of EY, GDY, MoP, and MG20 samples.

| Samples | $A_1$ (%) | $A_2$ (%) | $T_1$ (ns) | $T_2$ (ns) | $T_{ave}$ (ns) | $X^2$ |
|---------|-----------|-----------|------------|------------|----------------|-------|
| EY | 89.29 | 10.71 | 1.11 | 2.16 | 1.17 | 1.14 |
| GDY | 64.60 | 35.40 | 0.99 | 1.67 | 1.16 | 1.46 |
| MoP | 82.82 | 17.18 | 1.07 | 1.90 | 1.15 | 1.20 |
| MG20 | 98.25 | 1.75 | 1.21 | 4.17 | 1.22 | 1.24 |

GDY, the position of the energy band structure of MoP and GDY was understood. The flat-band potentials ($E_f$) were tested through the electrode sheets of GDY and MoP, and Ef winds of 0.38 and − 0.76 V were obtained for GDY and MoP, respectively (.

### 3.6. Density functional theory (DFT) calculations

The theoretical energy band structure between the monolayer GDY and MoP was further investigated by using DFT (density flooding theory) calculations, and the models of monolayer GDY and MoP were established for DFT calculations. [31,58]. This makes the MG catalyst belongs to the combination of topological semimetal and topological insulator, and the enhancement of the interaction force between the two, in the light-excited state, electrons are more inclined with MoP [59].

### 3.7. Possible photocatalytic mechanisms

The surface potential of MoP and MG20 was tested by Kelvin probe force microscopy experiments, and by selecting smaller MoP particles (.

In order to further prove the possible mechanism between MoP and GDY, in situ XPS experiment was used as a basis for determining photogenerated electron transfer between catalysts, and EPR (DMPO-·O$_2^-$) experiment was used as the change of reducing ability of catalysts. The fitted peaks shown in the in situ XPS of the MG20 have already been described in detail in the 3.2 section, so we will not go into too much detail. Through the local enlargement in Fig. 12(a-d), we can clearly see that the binding energy of sp$^2$ and sp orbits in GDY increases, and the binding energy of Mo-P, Mo-O and P-O bonds in MoP decreases[66,67]. It is judged that photogenerated electrons generated by GDY in MG may be transferred to MoP under light conditions. It can be seen from Fig. 12 (e,f) that no significant DMPO signal was observed for MoP, GDY and MG20 catalysts under dark conditions. MoP, GDY and MG20 showed obvious DMPO-·O$_2^-$ characteristic signals after 2 min of illumination, and according to the displayed spectral intensity, MG20 had stronger reduction ability, followed by MoP and GDY the lowest, proving that MG20 retained a higher reduction potential. At the same time, an interesting phenomenon can be found, the spectral trend of MG20's DMPO-·O$_2^-$ is consistent with MoP, but at 3495.60 and 3509.10 G, it can be clearly found that the peak position of GDY and MG20 is consistent, which has a certain supporting effect on the success of MG20 preparation from the side.

Penman propose a possible photocatalytic mechanism for MG by combining the energy band structures of MoP and GDY. As shown in Fig. 13(a, b), the contact surfaces of MoP and GDY lead to the equilibrium of Fermi energy levels at the contact surface due to the different
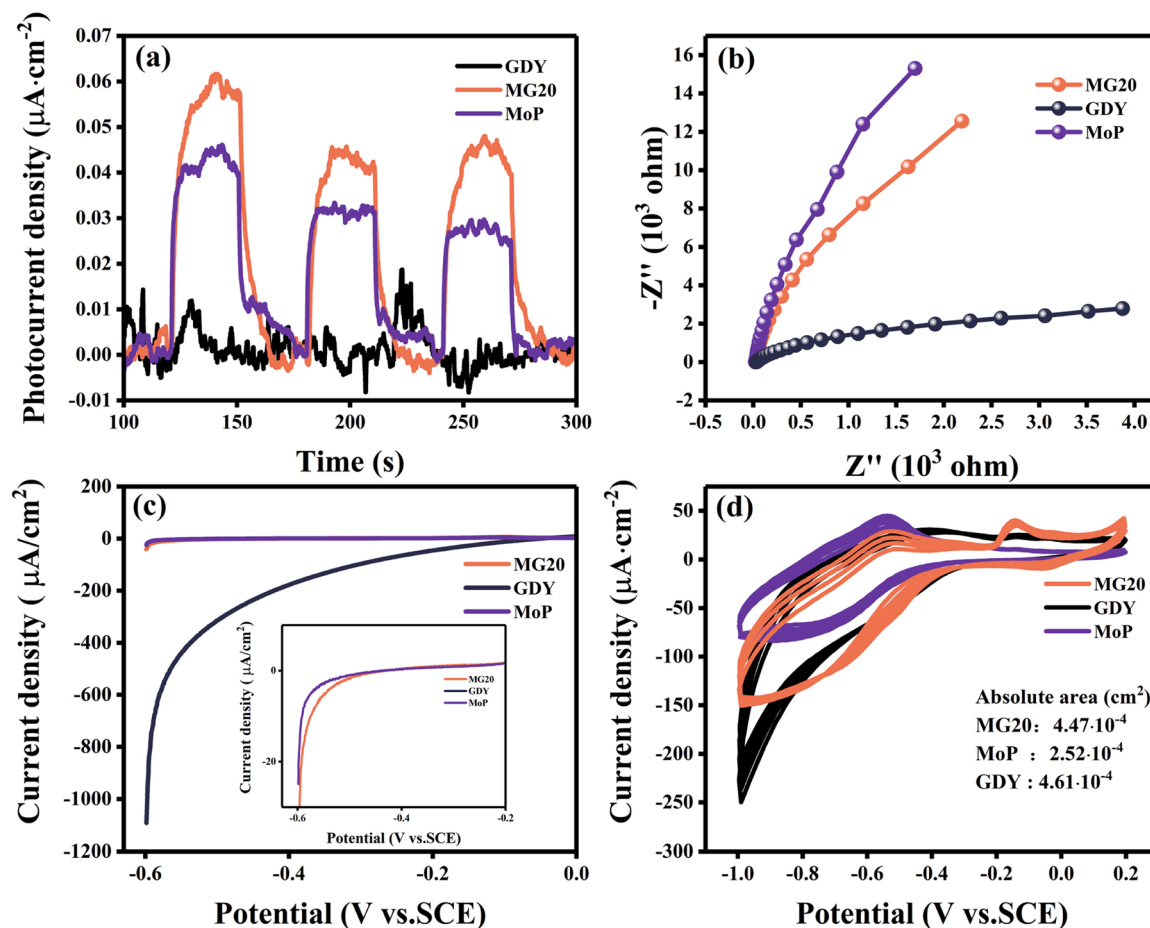
**Fig. 8.** (a) Transient photocurrent response; (b) Nyquist plots of electrochemical impedance spectroscopy; (c)Linear scanning voltammetric curves; (d) Cyclic voltammetric curves.
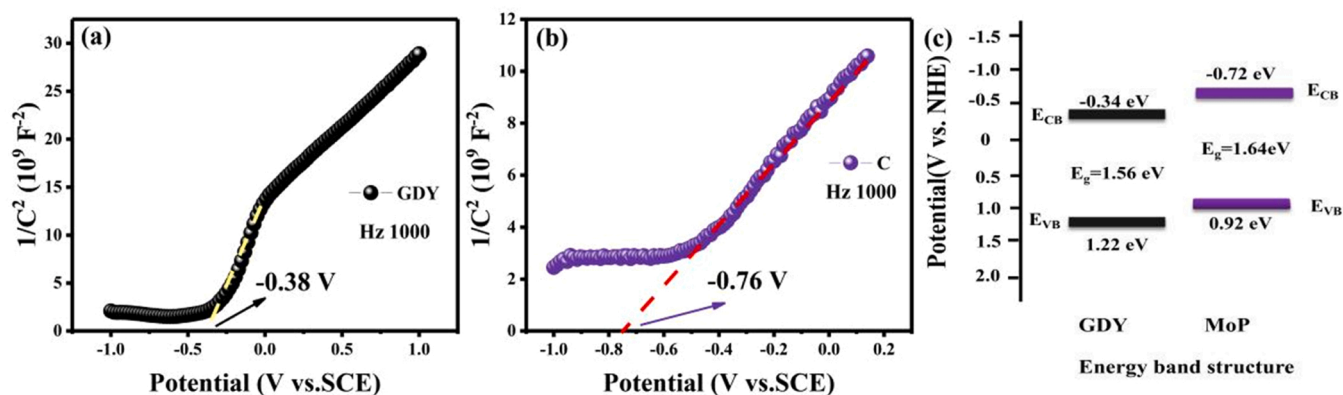


**Fig. 9.** (a, b) Mott-Schottky plots of GDY and MoP; (c) Energy band structure of MG.

Fermi energy levels of the two substances, which leads to the energy band bending and hinders the electron shift. The Emerging S-Scheme Photocatalyst published by zhang et al. in 2022 is presented as one the evidence for the schematic of hydrogen production under the MG composite catalyst EY photosensitizer (Fig. 13(b)) [5]. Under the irradiation of 5 W LED simulating visible sunlight, electrons on GDY and MoP VB are excited to CB to form a photogenerated electrons-holes. Photogenerated electrons from GDY migrate to VB of MoP to complex with holes generated by MoP. At the same time, TEOA can consume holes generated on GDY VB, which is beneficial to reducing the complexation of photogenerated carriers and further improving the hydrogen evolution of the catalyst. The EY is excited to form an $EY^{1*}$ which is converted to the more stable $EY^{3*}$ via ISC ($EY^{3*}$ gains electrons from TEOA to generate $EY^-$ radicals. $EY^-$ has a strong oxidation capacity and eventually passes electrons to the CB of MG20 to participate in the hydrogen evolution reaction [68–74].
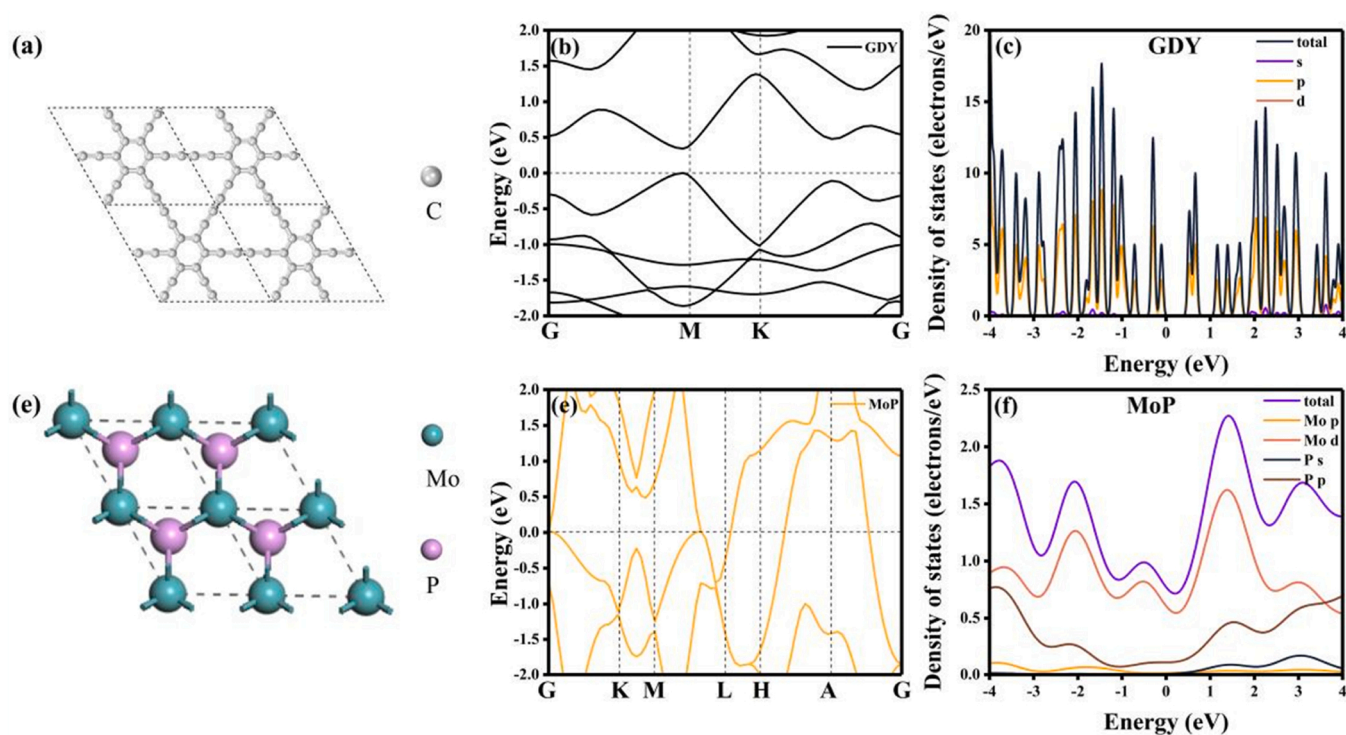
**Fig. 10.** (a, e) The unit cell of GDY and MoP, (b, e) band structure of GDY and MoP, (c, f) densities of states of GDY and MoP.
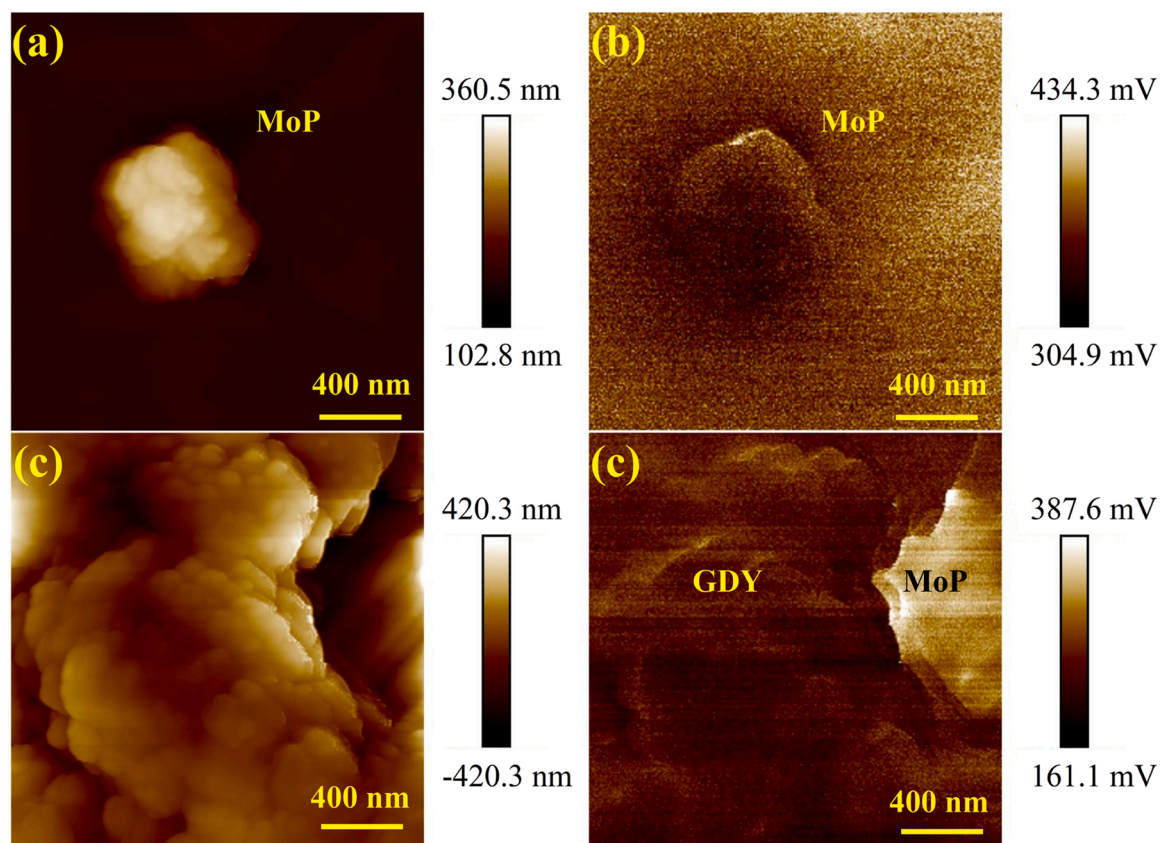


**Fig. 11.** (a) Highly sensing image of MoP, (b) KPFM image of MoP, (c) Highly sensing image of MG20, (d) KPFM image of MG20.
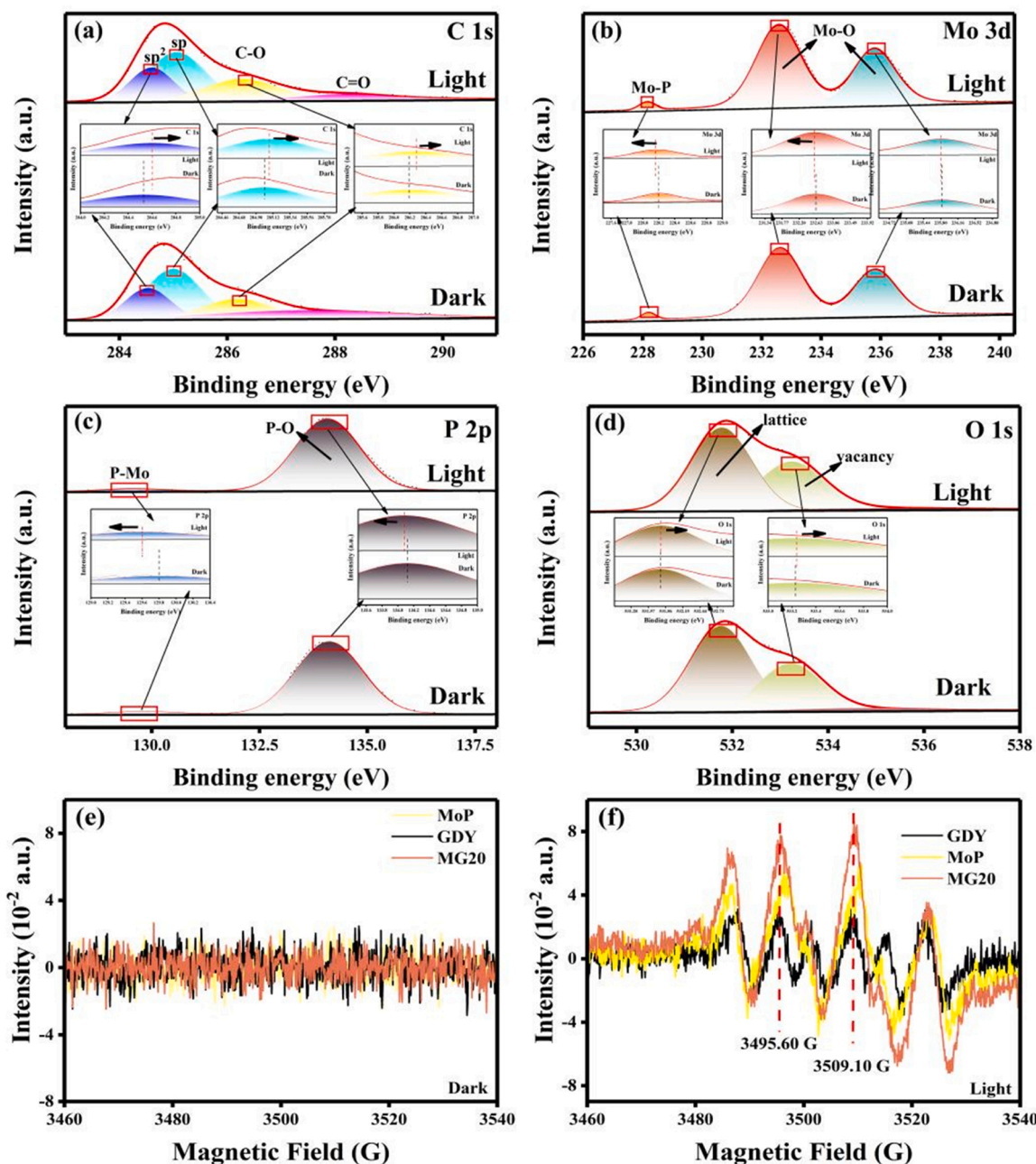
**Fig. 12.** (a-d) XPS spectra of MG20; (e, f); EPR (DMPO-·O$_2$) experiment spectra in dark and light conditions.

## 4. Conclusions

In summary, a novel preparation strategy of graphdiyne (C$_n$H$_{2n-2}$) by one-pot conjugation and S-Scheme heterojunctions formed with MoP for efficiently photocatalytic hydrogen evolution. In the dye-sensitized system (pH=10; 15 vol% triethanolamine; 10 mg EY) could reach 443.82 μmol (8876.4 μmol·g$^{-1}$·h$^{-1}$) H$_2$ in 5 h, which is 11.82 and 1.99 times higher than that of GDY and MoP under the same conditions. There are two main reasons for the improved performance of MG20: on the one hand, the S-shceme heterojunction between GDY and MoP promotes the photogenerated electrons-holes separation and shortens the charge transfer distance; on the other hand, GDY has a unique atomic arrangement and a two-dimensional network of sp and sp$^2$ conjugated hybridization, and GDY has a natural advantage in constructing active catalytic sites. Meanwhile, its special charge distribution gives GDY the ability to be an electron acceptor or donor. This work presents a facile preparation method for GDY and also provides some ideas for GDY to enhance the hydrogen evolution of expired transition metal phosphides.

## CRediT authorship contribution statement

Youlin Wu and Zhiliang Jin designed this experiment; Youlin Wu investigated; Zhiliang Jin provided reagents, materials, and analytical tools; Youlin Wu wrote the article.

## Declaration of Competing Interest

The authors declare that they have no known competing financial interests or personal relationships that could have appeared to influence the work reported in this paper.
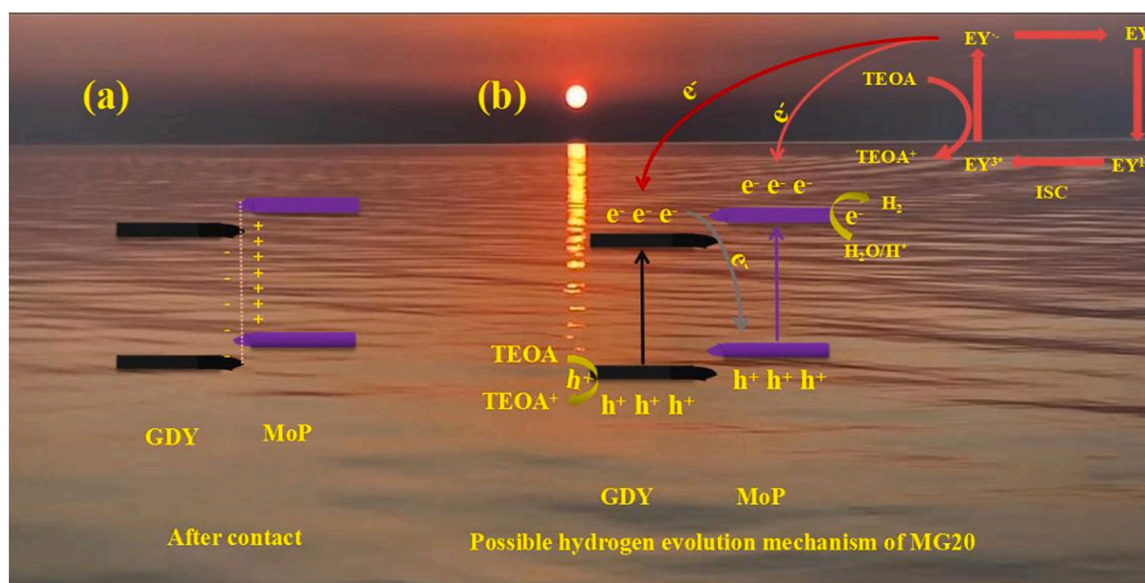
**Fig. 13.** (a) After contract; (b)The possible mechanism after contact with MG.

## Data Availability

No data was used for the research described in the article.

## Acknowledgments

## References

[1] L. Zhang, J. Zhang, H. Yu, J. Yu, Emerging S-scheme photocatalyst, Adv. Mater. 34 (2021), 2107668.

[2] Q. Xu, L. Zhang, B. Cheng, J. Fan, J. Yu, S-scheme heterojunction photocatalyst, Chem 6 (2020) 1543–1559.

[3] F. Xu, K. Meng, B. Cheng, S. Wang, J. Xu, J. Yu, Unique S-scheme heterojunctions in self-assembled $TiO_2/CsPbBr_3$ hybrids for $CO_2$ photoreduction, Nat. Commun. 11 (2020) 4613.

[4] L. Wang, Y. Li, C. Wu, X. Li, G. Shao, P. Zhang, Tracking charge transfer pathways in $SrTiO_3/CoP/Mo_2C$ nanofibers for enhanced photocatalytic solar fuel production, Chin. J. Ctaalysis 43 (2022) 507–518.

[5] Z. Jin, L. Zhang, Performance of Ni-Cu bimetallic co-catalyst g-$C_3N_4$ nanosheets for improving hydrogen evolution, J. Mater. Sci. Technol. 49 (2020) 144–156.

[6] Y. Bao, S. Song, G. Yao, S. Jiang, S-scheme photocatalytic systems, Sol. RRL 5 (2021), 2100118.

[7] Z. Jin, Y. Li, X. Hao, Ni, Co-based selenide anchored g-$C_3N_4$ for boosting photocatalytic hydrogen, Evolution 37 (2021), 1912033.

[8] M. Sun, J. Hu, C. Zhai, M. Zhu, J. Pan, CuI as hole-transport channel for enhancing photoelectrocatalytic activity by constructing CuI/BiOI heterojunction, ACS Appl. Mater. Interfaces 9 (2017) 13223–13230.

[9] D.H. Seo, S.Y. Hong, T.H. You, A. Sivanantham, I.S. Cho, Using a $CeO_2$ quantum dot hole extraction-layer for enhanced solar water splitting activity of BiVO4 photoanodes, Chem. Eng. J. 450 (2022), 137917.

[10] K. He, R. Shen, L. Hao, Y. Li, P. Zhang, J. Jiang, L. Xin, Advances in nanostructured silicon carbide photocatalysts, Acta Phys. Chim. Sin. 0 (2022), 2201021.

[11] L. Zhang, Y. Wu, J. Li, Z. Jin, Y. Li, N. Tsubaki, Amorphous/crystalline heterojunction interface driving the spatial separation of charge carriers for efficient photocatalytic hydrogen evolution, Mater. Today Phys. 27 (2022), 100767.

[12] Z. Jiang, B. Cheng, Y. Zhang, S. Wageh, A.A. Al-Ghamdi, J. Yu, L. Wang, S-scheme ZnO/WO3 heterojunction photocatalyst for efficient $H_2O_2$ production, J. Mater. Sci. Technol. 124 (2022) 193–201.

[13] M. Sayed, J. Yu, G. Liu, M. Jaroniec, Non-noble plasmonic metal-based photocatalysts, Chem. Rev. 122 (2022) 10484–10537.

[14] Y. Zhang, X. Zhang, S. Silva, B. Ding, P. Zhang, G. Shao, Lithiumve plasmonic metal-based photocatalystsfor efficient hatial separation of charge carriers for efficient photocatalytic hydrogen evolutin, Science 9 (2022), 2103879.

[15] X. Wang, Y. Li, T. Li, Z. Jin, Synergistic effect of bimetallic sulfide enhances the performance of CdS photocatalytic hydrogen evolution, Adv. Sustain. Syst. (2022), https://doi.org/10.1002/adsu.202200139.

[16] L. Zhang, Z. Jin, N. Tsubaki, Activating and optimizing the $MoS_2@MoO_3$ s-scheme heterojunction catalyst through interface engineering to form a sulfur-rich surface for photocatalyst hydrogen evolution, Chem. Eng. J. 438 (2022), 135238.

[17] N. Tang, Y. Li, F. Chen, Z. Han, In situ fabrication of a direct Z-scheme photocatalyst by immobilizing CdS quantum dots in the channels of graphene-hybridized and supported mesoporous titanium nanocrystals for high photocatalytic performance under visible light†, RSC Adv. 8 (2018) 42233–42245.

[18] J. Li, M. Li, Y. Li, X. Guo, Z. Jin, Lotus-leaf-like $Bi_2O_2CO_3$ nanosheet combined with $Mo_2S_3$ for higher photocatalytic hydrogen evolution, Sep. Purif. Technol. 288 (2022), 120588.

[19] P. Chen, F. Liu, H. Ding, S. Chen, L. Chen, Y.-J. Li, C.-T. Au, S.-F. Yin, Porous double-shell [email protected]$_3N_4$ octahedron derived by in situ supramolecular self-assembly for enhanced photocatalytic activity, Appl. Catal. B: Environ. 252 (2019) 33–40.

[20] Z. Jin, X. Jiang, X. Guo, Hollow tubular $Co_9S_8$ grown on $In_2O_3$ to form S-scheme heterojunction for efficient and stable hydrogen evolution, Int. J. Hydrog. Energy 47 (2021) 1669–1682.

[21] Y. Yang, B. Cheng, J. Yu, L. Wang, W. Ho, $TiO_2/In_2S_3$ S-scheme photocatalyst with enhanced $H_2O_2$-production activity, Nano Res. (2021), https://doi.org/10.1007/s12274-021-3733-0.

[22] Q. Xu, S. Wageh, A.A. Al-Ghamdi, X. Li, Design principle of S-scheme heterojunction photocatalyst, J. Mater. Sci. Technol. 124 (2022) 171–173.

[23] S. Liu, K. Wang, M. Yang, Z. Jin, Rationally designed $Mn_{0.2}Cd_{0.8}$S@CoAl LDH S-scheme heterojunction for efficient photocatalytic hydrogen production, Acta Phys. Chim. Sin. 0 (2021), 2109023-2109020.

[24] S. Wageh, A.A. Al-Ghamdi, R. Jafer, X. Li, P. Zhangc, A new heterojunction in photocatalysis: S-scheme heterojunction, Chin. J. Catal. 42 (2021) 667–669.

[25] D. Li, X. Mai, P. Su, S. Yangg, Z. Jiang, Y. Li, Z. Jin, Effect of phosphating on NiAl-LDH layered double hydroxide form S-scheme heterojunction for photocatalytic hydrogen evolution, Mol. Catal. 516 (2021), 111990.

[26] Y. Zhang, P. Zhang, S. Zhang, Z. Wang, N. Li, S. Silva, G. Shao, A flexible metallic TiC nanofiber/vertical graphene 1D/2D heterostructured as active electrocatalyst for advanced Li-S batteries, InfoMat 3 (2021) 790–803.

[27] P. Zhang, Y. Li, X. Li, Solar to $H_2O_2$ in-situ generation and utilization: a self-cyclable photocatalytic Fenton-like system, Chin. J. Catal. (2022) 43, https://doi.org/10.1016/S1872-2067(22)64185-8.

[28] H. Li, G. Wang, X. Zhang, Z. Jin, Based on amorphous carbon C@ZnxCd1-xS/Co$_3$O$_4$ composite for efficient photocatalytic hydrogen evolution, Int. J. Hydrog. Energy 45 (2020) 8405–8417.

[29] L. Zhang, X. Hao, J. Li, Y. Wang, Z. Jin, Unique synergistic effects of ZIF-9(Co)-derived cobalt phosphide and $CeVO_4$ heterojunction for efficient hydrogen evolution, Chin. J. Catal. 41 (2020) 82–94.

[30] G. Wang, Y. Quan, K. Yang, Z. Jin, EDA-assisted synthesis of multifunctional snowflake-$Cu_2$S/CdZnS S-scheme heterojunction for improved the photocatalytic hydrogen evolution, J. Mater. Sci. Technol. 121 (2022) 28–39.

[31] T. Li, L. Zhang, X. Wang, X. Li, Z. Jin, Design and synthesis of phosphating bimetallic CeCo-MOF for substantially improved photocatalytic hydrogen evolution, J. Mater. Chem. C. 10 (2022) 8750–8761.

[32] Z. Jin, M. Yang, X. Hao, P. Zhu, ZIF-67 dodecahedron coupled with CoAl-layered double hydroxide as S-scheme heterojunction for efficient visible-light-driven hydrogen evolution, Appl. Surf. Sci. 592 (2022), 153300.

[33] T. Li, Y. Li, Z. Jin, Surface-induced engineering: P-induced formation of surface bonding states based on the ZIF synthesis strategy for photocatalytic hydrogen evolution, Inorg. Chem. 61 (2022) 12809–12821.

[34] F. Yang, D. Liu, Y. Li, S. Ning, L. Cheng, J. Ye, Solid-state synthesis of ultra-small freestanding amorphous MoP quantum dots for highly efficient photocatalytic H2 production, Chem. Eng. J. 406 (2021), 126838.

[35] L. Zhang, Z. Jin, N. Tsubaki, MoP@MoO$_3$ S-scheme heterojunction in situ construction with phosphating MoO$_3$ for high-efficient photocatalytic hydrogen production, Nanoscale 13 (2021) 18507–18519.

[36] X. Jiang, M. Fuji, Facile preparation of nanosized MoP as cocatalyst coupled with TiO$_2$ for highly efficient photocatalytic H2 production, Catal. Lett. (2022), https://doi.org/10.1007/s1056-021-0388-y.

[37] T. Yan, H. Liu, Z. Jin, Graphdiyne based ternary GD-CuI-NiTiO$_3$ S-scheme heterjunction photocatalyst for hydrogen evolution, ACS Appl. Mater. Interfaces 13 (2021) 24896–24906.

[38] G. Hu, J. He, Y. Li, Controllable synthesis of two-dimensional graphdiyne films catalyzed by a copper(II) trichloro complex, ACS Catal. 12 (2022) 6712–6721.

[39] Y. Liu, X. Ma, X. Jiang, Z. Jin, Phosphorus-modified two-dimensional graphdiyne (C$_n$H$_{2n-2}$)/ZnCdS forms S-scheme heterojunctions for photocatalytic hydrogen production, Nanoscale (2022), https://doi.org/10.1039/d2nr02671f.

[40] J. Li, M. Li, H. Li, Z. Jin, Novel CuBr-assisted graphdiyne synthesis strategy and application for efficient photocatalytic hydrogen evolution, J. Mater. Chem. C. 10 (2022) 2181–2193.

[41] Z. Jin, L. Zhang, G. Wang, Y. Li, Y. Wang, Graphdiyne formed a novel CuI-GD/g-C$_3$N$_4$ S-scheme heterojunction composite for efficient photocatalytic hydrogen evolution, Sustain. Energy Fuels 4 (2020) 5088–5101.

[42] G. Li, Y. Li, H. Liu, Y. Guo, Y. Li, D. Zhu, Architecture of graphdiyne nanoscale films, Chem. Commun. 46 (2010) 3256–3258.

[43] Q. Li, Y. Li, Y. Chen, L. Wu, C. Yang, X. Cui, Synthesis of γ-graphyne by mechanochemistry and its electronic structure, Carbon 138 (2018) 248–254.

[44] J. Zou, G. Liao, J. Jiang, Z. Xiong, S. Bai, H. Wang, P. Wu, P. Zhang, X. Li, In-situ construction of sulfur-doped g-C$_3$N$_4$/defective g-C$_3$N$_4$ isotype step-scheme heterojunction for boosting photocatalytic H$_2$ evolution, Chin. J. Struct. Chem. 41 (2022) 2201025–2201033.

[45] Y. Cao, H. Gou, P. Zhu, Z. Jin, Ingenious design of CoAl-LDH p-n heterojunction based on CuI as holes receptor for photocatalytic hydrogen evolution, Chin. J. Struct. Chem. 41 (2022) 2206079–2206085.

[46] Z. Jin, X. Wang, X. Hao, G. Wang, X. Guo, K. Wang, Graphdiyne based GDY/CuI/NiO parallel double S-scheme heterojunction for efficient photocatalytic hydrogen evolution, 2D Mater. (2022), https://doi.org/10.1088/2053-1583/ac5462.

[47] Z. Jin, H. Gong, A new allotrope of carbon—Graphdiyne (g-C$_n$H$_{2n-2}$) boosting with Mn0.2Cd0.8S form S-scheme heterojunction for efficient photocatalytic hydrogen evolution, Adv. Mterials Interfaces 8 (2021), 2100630.

[48] D. Xiang, X. Hao, X. Guo, G. Wang, K. Yang, Z. Jin, Rational Construction of Z-Scheme Charge Transfer Based on 2D Graphdiyne (g-CnH2n-2) Coupling with Amorphous Co3O4 Quantum Dots for Efficient Photocatalytic Hydrogen Generation, 2022, doi:10.1002/admi.202201400.

[49] G. Wang, Y. Quan, X. Hao, X. Guo, Z. Jin, Strong redox-capable graphdiyne-based double S-scheme heterojunction 10%GC/Mo for enhanced photocatalytic hydrogen evolution, 2022, doi:101016/j.jece.2022.109119.

[50] Z. Jin, X. Li, T. Li, Y. Li, Graphdiyne (C$_n$H$_{2n-2}$)-Based GDY/CuI/MIL-53(Al) S-Scheme Heterojunction for Efficient Hydrogen, Evolution (2022), https://doi.org/10.1021/acs.langmuir.2c02334.

[51] M. Yang, P. Wang, Y. Li, S. Tang, X. Lin, H. Zhang, Z. Zhu, F. Chen, Graphene aerogel-based NiAl-LDH/g-C$_3$N$_4$ with ultratight sheet-sheet heterojunction for excellent visible-light photocatalytic activity of CO$_2$ reduction, Appl. Catal. B: Environ. 306 (2022) 121065.

[52] K. Yang, T. Liu, D. Xiang, Y. Li, Z. Jin, Graphdiyne (g-C$_n$H$_{2n-2}$) based Co$_3$S$_4$ anchoring and edge-covalently modification coupled with carbon-defects g-C$_3$N$_4$ for photocatalytic hydrogen production, Sep. Purif. Technol. 298 (2022) 121564.

[53] Z. Jin, H. Li, J. Li, Efficient photocatalytic hydrogen evolution over graphdiyne boosted with a cobalt sulfide formed S-scheme heterojunction, Chin. J. Catal. 43 (2022) 303–315.

[54] L. Zhang, X. Hao, Y. Wang, Z. Jin, Q. Ma, Construction strategy of Mo-S@Mo-P heterojunction formed with in-situ phosphating Mo-S nanospheres toward efficient photocatalytic hydrogen production, Chem. Eng. J. 391 (2019), 123545.

[55] Y. Liu, X. Hao, H. Hu, Z. Jin, High efficiency electron transfer realized over NiS$_2$MoSe$_2$ S-scheme heterojunction in photocatalytic hydrogen, Evol., Acta Phys. Chim. Sin. 37 (2020), 2008030-2008030.

[56] J. Li, M. Li, Y. Li, X. Guo, Z. Jin, Lotus-leaf-like Bi$_2$O$_2$CO$_3$ nanosheet combined with Mo$_2$S$_3$ for higher photocatalytic hydrogen evolution, Sep. Purif. Technol. 288 (288) (2022), 120588.

[57] J. Peng, J. Shen, X. Yu, H. Tang, Q.Liu Zulfiqar, Construction of LSPR-enhanced 0D/2D CdS/MoO$_3$ S-scheme heterojunctions for visible-light-driven photocatalytic H$_2$ evolution, Chin. J. Catal. 42 (2021) 87–96.

[58] T. Yan, X. Zhang, H. Liu, Z. Jin, CeO$_2$ particles anchored to Ni$_2$P nanoplate for efficient photo-catalytic hydrogen, Evol., Chin. J. stuctural Chem. 41 (2022) 2201047–2201053.

[59] Y. Li, Z. Jin, L. Zhang, K. Fan, Controllable design of Zn-Ni-P on g-C$_3$N$_4$ for efficient photocatalytic hydrogen production, Chin. J. Catal. 40 (2019) 390–402.

[60] H. Li, H. Gong, Z. Jin, In$_2$O$_3$-modified three-dimensional nanoflower MoS$_x$ form S-scheme heterojunction for efficient hydrogen production, Acta Phys. Chim. Sin. 0 (2022), 2201037-2201030.

[61] J. Zhang, H. Liao, S. Sun, Construction of 1D/1D WO$_3$ nanorod/TiO$_2$ nanobelt hybrid heterostructure for photocatalytic application, Chin. J. stuctural Chem. 39 (2020) 1019–1028.

[62] H. Gong, Y. Li, H. Li, Z. Jin, 2D CeO$_2$ and a partially phosphated 2D Ni-based metal–organic framework formed an S-scheme heterojunction for efficient photocatalytic hydrogen evolution, Langmuir 38 (2022) 2117–2131.

[63] X. Lin, S. Du, C. Li, G. Li, Y. Li, F. Chen, P. Fang, Consciously constructing the robust NiS/g-C$_3$N$_4$ hybrids for enhanced photocatalytic hydrogen evolution, Catal. Lett. (2020).

[64] Y. Jiang, Y. Mao, Y. Jiang, H. Liu, W. Shen, M. Li, R. He, Atomic equidistribution enhanced RuIr electrocatalysts for overall water splitting in the whole pH range, Chem. Eng. J. 150 (2022) 189–1908.

[65] L. Xiao, Q. Zhang, P. Chen, L. Chen, F. Ding, J. Tang, Y. Li, C. Au, S. Yin, Copper-mediated metal-organic framework as efficient photocatalyst for the partial oxidation of aromatic alcohols under visible-light irradiation: synergism of plasmonic effect and schottky junction, Appl. Catal. B: Environ. 248 (2019) 380–387.

[66] X. Sheng, C. Chen, H. Liu, Z. Chen, Z. Yu, Y. Zhao, S. Yang, Two-dimensional second-order topological insulator in graphdiyne, Phys. Rev. Lett. 123 (2019), 256402.

[67] G. Li, Q. Xu, W. Shi, C. Fu, L. Jiao, M.E. Kamminga, M. Yu, H. Tüysüz, Ni Kumar, V. Süß, R. Saha, A.K. Srivastava, S. Wirth, G. Auffermann, J. Gooth, S. Parkin, Y. Sun, E. Liu, C. Felser, Surface states in bulk single crystal of topological semimetal Co$_3$Sn$_2$S$_2$ toward water oxidation, Sci. Adv. (2019) 5, https://doi.org/10.1126/sciadv.aaw9867.

[68] P. Zhang, Y. Li, Y. Zhang, R. Hou, X. Zhang, C. Xue, S. Wang, B. Zhu, N. Li, G. Shao, Photogenerated electron transfer process in heterojunctions: in situ irradiation XPS, Small Methods 4 (2020), 202000214.

[69] Y. Li, L. Wang, F. Zhang, W. Zhang, G. Shao, P. Zhang, Detecting and quantifying wavelength-dependent electrons transfer in heterostructure catalyst via in situ irradiation XPS, Adv. Sci. (2022), 2205020.

[70] Y. Zhang, Z. Wu, S. Wang, N. Li, S. Ravi, P. Silva, P. Zhang, Complex permittivity-dependent plasma confinement-assisted growth of asymmetric vertical graphene nanofiber membrane for high-performance Li-S full cells, InfoMat (2022), https://doi.org/10.1002/inf2.12294.

[71] H. Gong, Y. Li, H. Li, Z. Jin, 2D CeO$_2$ and partial phosphated 2D Ni-based metal-organic framework formed S-scheme heterojunction for efficient photocatalytic hydrogen evolution, Langmuir 38 (2022) 2117–2131.

[72] J. Li, M. li, Y. Li, X. Guo, Z. Jin, Lotus-leaf-like Bi$_2$O$_2$CO$_3$ nanosheet combined with Mo$_2$S$_3$ for higher photocatalytic hydrogen evolution, Sep. Purif. Technol. 288 (2022), 120588.

[73] Z. Fan, X. Zhang, Y. Li, X. Guo, Z. Jin, Construct 3D NiCo-LDH/Cu$_2$O p-n heterojunction via electrostatic self-assembly for enhanced photocatalytic hydrogen evolution, J. Ind. Eng. Chem. 110 (2022) 491–502.

[74] R. Hou, S. Zhang, Y. Zhang, N. Li, S. Wang, B. Ding, P. Zhang, A. three-region configuration for enhanced electrochemical kinetics and high-areal capacity lithium–sulfur batteries, Adv. Funct. Mater. (2022), 202200302.